Commissioning of a Two-Target DC Cylindrical Magnetron Sputter Coater for Depositing Nb_3Sn Film on Nb Superconducting Radiofrequency Cavities

Md Sharifuzzaman Shakel[1,2], Md Nizam Sayeed[1,2], Grigory V. Eremeev[3], Anne-Marie Valente-Feliciano[4], Uttar Pudasaini[4], and Hani E. Elsayed-Ali[1,2*]

[1]*Department of Electrical and Computer Engineering, Old Dominion University, Norfolk, VA 23529, USA*

[2]*Applied Research Center, 12050 Jefferson Avenue, Newport News, VA 23606, USA*

[3]*Fermi National Accelerator Laboratory, Batavia, IL 60510, USA*

[4]*Thomas Jefferson National Accelerator Facility, Newport News, VA 23606, USA*

A DC cylindrical magnetron sputter coater was commissioned and used to coat Nb 2.6 GHz superconducting radiofrequency (SRF) cavity with Nb_3Sn. The sputter coater has two identical cylindrical magnetrons that can move, with a controlled speed, along the axis of the SRF cavity to coat the inside surface of the cavity. The design of the sputter coater is discussed along with its performance. Initially, a sample holder that allows coating on flat substrates at positions similar to the equator and beam tubes of 2.6 GHz SRF cavity was used to test conditions for fabricating Nb_3Sn layers. Multilayers of Nb and Sn were sequentially sputtered on flat Nb and sapphire substrates mounted on the equivalent positions of the cavity's beam tubes and the equator using the two identical cylindrical magnetrons. Then, the Nb/Sn multilayers were annealed at 950 ºC for 3 hours. The ~1.2 μm thick Nb_3Sn film did not show any other Nb-Sn compounds and had a superconducting transition temperature of 17.61–17.76 K. The 2.6 GHz SRF cavity was coated using similar conditions as flat samples. Cryogenic RF testing of the Nb_3Sn-coated cavity demonstrated a quality factor of 3.2×10^8 at an accelerating gradient of 5 MV/m at 4.4 K.

Keywords: Nb_3Sn thin film; cylindrical magnetron sputtering; structure; superconducting properties

* Corresponding author: helsayed@odu.edu.

1. Introduction

Superconducting radiofrequency (SRF) cavities are the key part of many existing and planned particle accelerators, such as XFEL, CEBAF, LCLS-II, PIP-II, EIC, and FCC-ee [1–6]. The RF properties of the cavity, hence its operational efficiency and performance, depend on the quality of its inner surface. Up to now, Nb has been the material of choice for SRF cavity fabrication due to its highest superconducting critical temperature (T_c ~9.25 K) and highest superheating magnetic field (H_{sh} ~200 mT) among all the pure metals and for the ease of fabrication and use [7,8]. The surface preparation of Nb cavities has advanced significantly over the last few decades, bringing the performance of Nb cavities, in terms of H_{sh} and operating temperature, close to the intrinsic limit [9–11]. Hence, alternative materials with superior superconducting properties are researched to develop enabling technologies for accelerator structures [12]. Nb_3Sn is considered one of the most promising materials for SRF cavities due to its higher T_c ~18.3 K and H_{sh} ~400 mT, which is almost twice that of Nb. Though Nb_3Sn coated cavities can achieve quality factor Q_o orders of magnitude higher than bulk Nb cavities at the same temperature, thus reducing the operating cost, the brittleness of Nb_3Sn and the complicated shape of SRF cavities make it technologically challenging to coat high quality Nb_3Sn films uniformly inside the cavities [13].

Methods used to fabricate Nb_3Sn thin films include Sn vapor deposition [14–17], co-deposition of Nb and Sn by thermal evaporation [18], Nb dipping into Sn liquid followed by thermal diffusion [19], electrochemical synthesis [20,21], bronze routes [22,23], and magnetron sputtering [24–31]. The best RF results with Nb_3Sn cavities have been achieved using vapor diffusion technique [13,15,32]. With the vapor diffusion technique Nb_3Sn thin film is grown on the inner surface of Nb SRF cavities by Sn vapor diffusion, when Nb surface is heated while exposed to Sn vapor [33]. While this coating technique has produced best results to-date, the RF results fall short of theoretical expectations with several potential causes identified, e.g., the resulting Nb_3Sn film often has Sn-deficient areas [17,34,35].

Magnetron sputtering followed by annealing is another promising method for Nb_3Sn film fabrication with broad control over stoichiometry and surface uniformity. Using magnetron sputtering followed by the annealing, the stoichiometry of the Nb_3Sn can be controlled by adjusting the thickness of the sputtered Nb and Sn layers [36]. Also, controlling the sputter deposition parameters with computerized automated magnetrons and modifying the plasma density near the substrate position can improve the surface quality of the film and allow it to coat complex-shaped objects uniformly [37]. Cylindrical magnetron sputtering has been used to deposit superconductive coatings into SRF cavities [38–40]. Cylindrical magnetrons can be operated with different magnetic field configurations (balanced and unbalanced) to achieve the desired plasma shape and density and allow control over the sputtering parameters [41].

We have commissioned a sputter coater with two identical DC cylindrical magnetrons of unbalanced magnetic configuration. Multilayers of Nb and Sn were sequentially sputtered on Nb and sapphire substrates mounted on positions replicating the beam tubes and equator of a 2.6 GHz Nb SRF cavity. The samples were annealed at 950 ^{o}C for 3 hours to form ~1.2 μm Nb_3Sn film. Nb_3Sn was coated on the inside surface of a 2.6 GHz Nb SRF cavity using the same deposition parameters. The design of the cylindrical magnetron system, along with the Nb_3Sn film characterization and SRF cavity performance, are discussed.

2. Design of the cylindrical magnetron sputtering system

2.1. Vacuum chamber

The custom-designed high vacuum chamber, shown in Figure 1, accommodates two identical cylindrical magnetrons. It consists of five 8-inch and two 4-inch Conflat flanges for inserting the magnetrons and connecting other vacuum components. The magnetrons are inserted vertically into the chamber through two 8-inch flanges, one from the top and another from the bottom. The vertical placement of the magnetrons inside the chamber is chosen to prevent the possibility of sagging if placed horizontally. The design has low angular tolerance (within 0.01") of the flanges to ensure that the magnetrons are placed and aligned with the axis of the cavity. The chamber is pumped down by a TPS-flexy turbo pumping system from Agilent Technologies and consists of an IDP-7 dry scroll roughing pump and a TwisTorr 305 FS turbo pump. The KJL-SPARC vacuum gauge from Kurt J. Lesker can measure pressure down to 7.6 $\times$ 10^{-10} torr using a cold cathode/Pirani gauge combination system. An MKS (model GE50A013501RMV020) gas flow controller calibrated to N_2 sets the gas flow rate in the chamber with a maximum rate of 50 SCCM. The baseline pressure of the chamber was maintained at ~1x10^{-8} Torr.

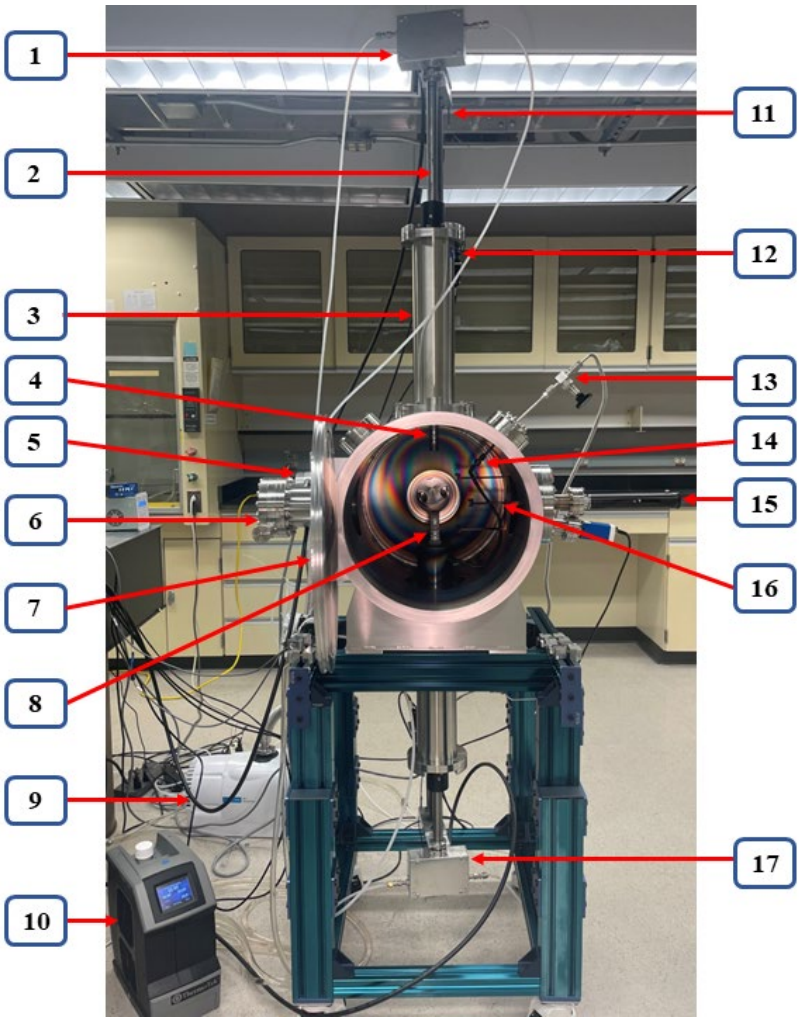

Fig. 1. DC cylindrical magnetron sputtering system: (1) water flow controller for the top magnetron; (2) top magnetron movement controller rod; (3) top magnetron shield; (4) Nb target installed on top magnetron; (5) turbomolecular pump; (6) viewport; (7) chamber door; (8) Sn target installed on bottom magnetron; (9) roughing pump; (10) chiller; (11) optical limit switch; (12) top magnetron movement controller motor; (13) gas feedthrough; (14) gas tube; (15) linear movement controller feedthrough; (16) flat sample holder; (17) water flow controller for the bottom magnetron.

2.2. Cylindrical magnetrons

The two identical cylindrical magnetrons were made by Plasmionique Inc, Canada [42]. Each consists of 4 cylindrical magnets (neodymium N55 grade) coated with Ni, Cu, and epoxy and separated by spacers. The magnets are arranged in a post-cathode magnetron configuration and have the same diameter (OD 16 mm × ID 4 mm), however, the outer two magnets are 7.74 mm in length while the two

middle magnets are 6.35 mm long. Figure 2 shows magnetic field measurement at the magnetron wall, at the target surface and ~8.5 mm away from the target surface. The magnetrons have similar magnetic field distribution along their axes. The magnetrons are water-cooled with a flow rate of ~l L/min using a thermoelectric recirculating chiller (ThermoTek T257P).

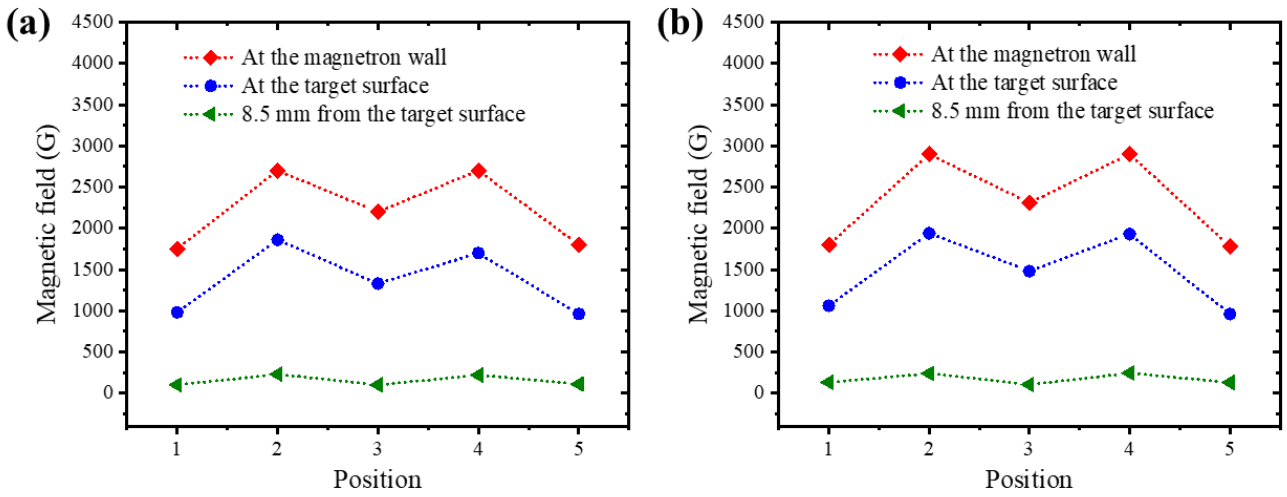

Fig. 2. Magnetic field distribution around (a) Top magnetron, and (b) Bottom magnetron measured at the magnetron walls, at the target surface and ~8.5 mm away from the target surface.

Each magnetron can travel ~280 mm from its home position. The highest moving speed for both magnetrons is 1.3 mm/s. A DC power supply from ADL (Model GS 10, Germany) capable of delivering DC output of 1 kW to power the magnetrons. A communication controller device (Plasmionique Inc. Model CO1000) is used for switching the DC power between the two magnetrons. A motor controller device (Plasmionique Inc. Model MC120) controls the magnetron movement. An automation software (Plasmionique Inc. SPT2C0) controls the sputter deposition process. The automation program selects the magnetron, sets desired DC power, current, or applied voltage of the discharge, sets the desired magnetron speed at different positions throughout the deposition region, and runs the deposition for a selected amount of time. The interlock feature of the magnetrons permits powering each magnetron only when the water

flow in the magnetron is above a safe flow rate and prevents accidental collision of the two magnetrons. The discharge power, voltage, and current values and the water flow rate are saved in a data log.

3. Optimization of deposition conditions for Nb_3Sn fabrication

3.1. Magnetron operation power for Nb and Sn deposition

To achieve uniform deposition of Nb and Sn layers on the surface of a SRF cavity, power applied to the magnetrons must generate stable and symmetric plasma with a known deposition rate at the equator and beam tubes. The magnetron plasma stability was tested at 10 mTorr Ar background pressure with a flow rate of 50 SCCM. An Nb tube target (0.9" OD × 0.8" ID × 4.5" long, 99.99% purity, from ACI ALLOYS Inc.) was installed on the magnetron. When operating the magnetron with the Nb target at a power of 2 to 17 W, the formed plasma rings were visibly asymmetrical. Figure 3(a) shows that for a magnetron power of 12 W, the bottom ring has a higher intensity than the other three rings. Several tests confirmed that, when 18 W or higher DC power is applied to the magnetron, the plasma ring intensities are visually almost symmetrical, with the intensity of the two middle rings lower than the two outer rings, as shown in Figure 3(b). During deposition, the magnetrons travel vertically many times along the SRF cavity. Therefore, the variation of the sputter rate from each ring averages out. Similar testing was performed for the magnetron operation with the Sn target. For Sn, operating the magnetron at 8 W resulted in a stable discharge for the four plasma rings around the target, as shown in Figure 3(c).

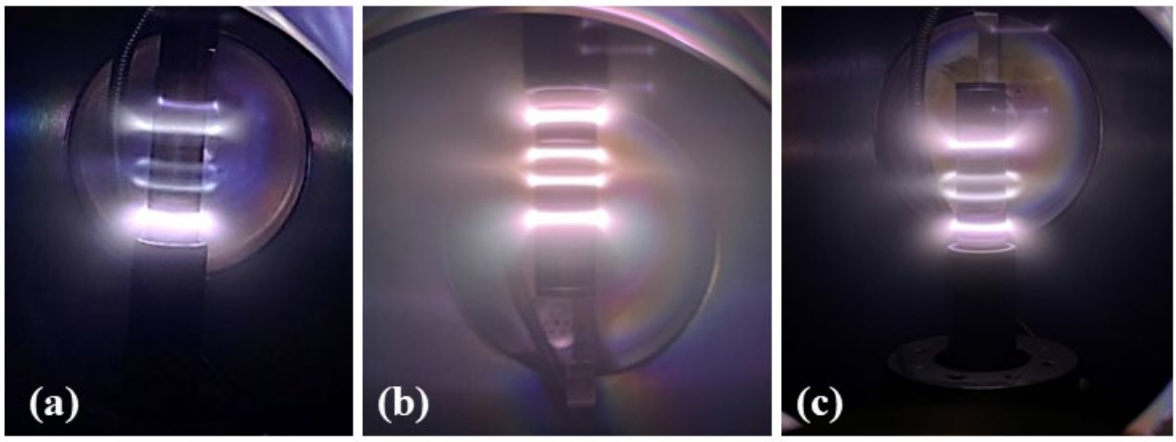

Fig. 3. Photographs of the operating cylindrical magnetron discharge; (a) Nb target with 12 W DC power produces visibly asymmetrical plasma intensity formation; (b) Nb target with 18 W DC power produces stable, almost symmetrical plasma formation; (c) Sn discharged by 8 W DC power produces stable and symmetrical plasma ring intensities.

3.1. Deposition rate calibration

The deposition rates of Nb and Sn are calibrated for the Nb tube target placed on the top magnetron and the Sn tube target placed on the bottom magnetron. A custom sample holder is used along with a linear feedthrough to mount three silicon substrates replicating three positions of a 2.6 GHz Nb SRF cavity: center of top beam tube, equator, and center of bottom beam tube. Both magnetrons with the Nb and Sn targets traveled vertically along the axis of the cylindrical sputtering chamber, which is also the axis of the SRF cavity when placed in the deposition chamber.

An automation program was used to move the magnetrons from their home position to the initial deposition position. Then, the program applies power to one of the magnetrons and initiates the magnetron movement with the selected travel speed that can be controlled along with the travel distance. After completing a selected number of magnetron passes, the program turns off the discharge. This sequence can then be repeated for the other magnetron to deposit multilayers for Nb and Sn.

For the Nb and Sn deposition rate calibration, 1 mm/s speed and 0.5 mm/s^2 acceleration are used for the magnetron movement. At the operation powers (30 W for Nb and 8 W for Sn), the Nb magnetron was allowed to complete 24 passes, while the Sn magnetron completed 48 passes. The thicknesses of the Nb and Sn films were checked by cross-sectional scanning electron microscopy (SEM) using JOEL JSM 6060 LV SEM. Based on the film thickness, each pass of the bottom magnetron (with the Sn target) deposited ~14, ~19, and ~14 nm Sn film at the center of the top beam tube, equator, and center of the bottom beam tube, respectively. The Nb deposition per pass was ~18, ~25, and ~16 nm at the center of the top beam tube, equator, and center of the bottom beam tube, respectively.

4. Coating on flat samples

4.1 Multilayer sequential sputtering of Nb and Sn

Flat Nb coupons (10 mm × 10 mm × 3 mm) were prepared from Nb slice (Tokyo Denkai Co., Japan, residual resistivity ratio (RRR) ~300) using electrical discharge machining. The samples were treated with buffered chemical polishing (BCP) to remove ~100 μm from the surface using a solution of volume ratio 1:1:1 of 49% HF, 70% HNO_3, and 85% H_3PO_4. Before mounting the Nb samples on the three positions simulating the centers of the top beam tube, equator, and the bottom beam tube of a 2.6 GHz SRF cavity, the samples were wiped with ethanol, then with acetone, and dried with air.

The fabrication of the Nb_3Sn film on Nb starts with the deposition of ~200 nm (at equator position) Nb buffer layer by having the top magnetron complete 8 passes covering the length of the SRF cavity. During annealing some of the Sn from the adjacent layer diffuses into the Nb buffer layer and this prevents high Sn concentration near the surface, therefore the evaporation of Sn and the growth of Sn rich particles on the surface also is reduced [43]. After deposition of the Nb buffer layer, 16 layers of ~25 nm Sn and ~50 nm Nb were sequentially deposited on the buffer layer, which gives a total ~1.2 μm thick film on the

equator position. The total film thickness on the top and bottom beam tubes were ~880 nm and ~816 nm, respectively. The speed of the magnetrons with Nb and Sn were 1.00 and 0.75 mm/s, respectively. The thicknesses of the Nb and Sn and the total film thickness are listed in Table 1. Figure 4 shows the magnetron current, which was ~23 mA when depositing the Sn layer using 8 W DC power and ~99 mA when depositing the Nb layer using 30 W DC power.

Table 1. The thickness of Nb and Sn layers, and the total thickness of the films at three locations replicating the 2.6 GHz Nb SRF cavity.

Position	Nb layer thickness (nm)	Sn layer thickness (nm)	Number of Nb and Sn layers each	Total thickness (nm)
Top beam tube	36	19	16	880
Equator	50	25		1200
Bottom beam tube	32	18		816

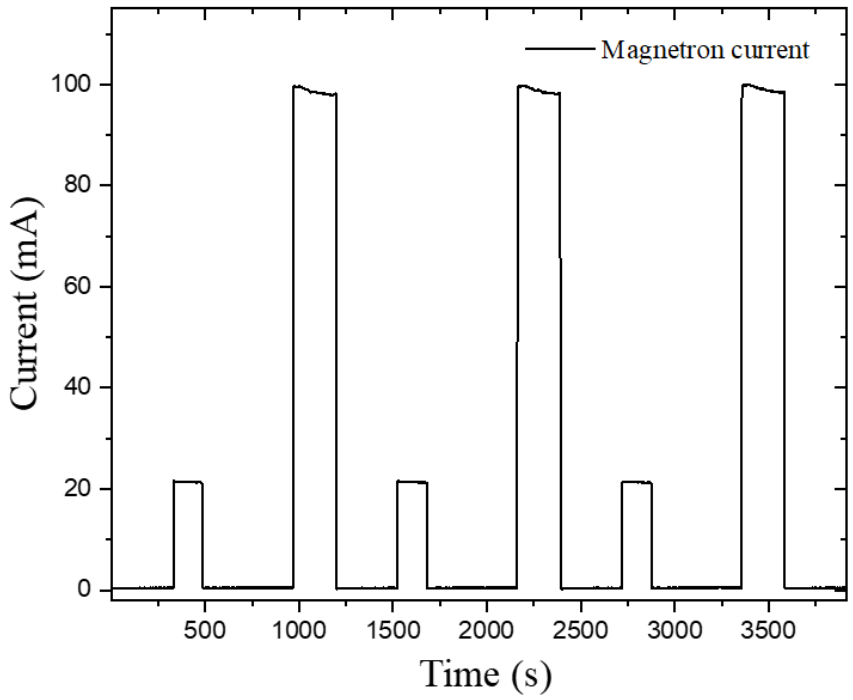

Fig. 4. Magnetron current during multilayer deposition showing 3 layers out of 16 of Sn and Nb. For the Sn layer deposition with 8 W, the current was ~21 mA and for the Nb layer deposition with 30 W, the current was ~99 mA.

4.2 Annealing

After sequentially depositing Sn and Nb layers, the samples were annealed at 950 ºC for 3 hours in a furnace with a temperature ramp rate of 12 ºC/min. The furnace has an insert made of Nb to load samples for annealing. The base pressure of the furnace is the mid 10^{-8} Torr. The insert is evacuated to ~10^{-6} Torr. The films were annealed by maintaining the desired annealing temperature for specific time. Annealing caused the diffusion and reaction of the Nb and Sn layers forming the Nb_3Sn layer.

4.3 Results

4.3.1 Structure

The crystal structures of the Nb_3Sn films deposited on Nb substrates are characterized by an X-ray diffractometer (Rigaku Miniflex II, Japan) using Cu-Kα radiation. X-ray diffraction (XRD) patterns of the as-deposited and annealed samples are shown in Figure 5. The XRD patterns of the three as-deposited samples have the Nb peaks (110), (200), (211), and (310). Only the XRD pattern of the sample at the top beam tube location has multiple Sn diffraction peaks (200), (101), (220), (112), and (400). No diffraction peaks of Nb_3Sn were observed for the as-deposited films. After the annealing, all three samples have the Nb_3Sn peaks (110), (200), (210), (211), (222), (320), (321), (400), (420), (421), and (332). The Nb peaks (200), (211), and (310) were also present in the XRD patterns of the annealed samples, which originate from the Nb substrate. No other phases of any intermetallic compound of Nb and Sn (i.e., Nb_6Sn_5 or $NbSn_2$) were observed in the XRD patterns of the annealed samples.

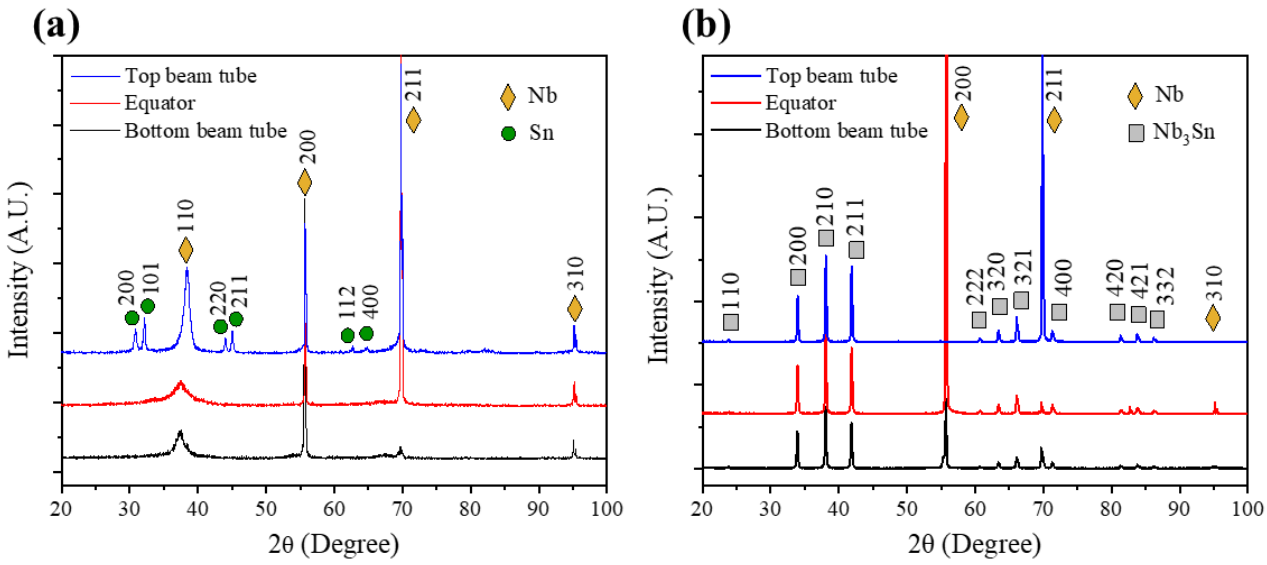

Fig. 5. X-ray diffraction patterns of the (a) as-deposited and (b) annealed films. The substrates were mounted at equivalent positions of the center of the two beam tubes and the equator of a 2.6 GHz Nb SRF cavity.

The full-width half maximum (FWHM) of the Nb_3Sn (200), (210), and (211) diffraction orders from the annealed samples were used to calculate the crystallite size of the films using the Scherrer equation. The sample on the equator position had the smallest crystallite size of ~35–40 nm. The crystalline size of the top beam tube was ~39–44 nm, while that of the bottom beam sample tube was ~38–43 nm.

4.3.2 Composition

The surface elemental composition of the as-deposited and annealed samples is characterized using a Noran 6 energy dispersive X-ray spectroscopy (EDX) detector connected to the JOEL JSM 6060 LV SEM. The electron energy used for EDX was 15 kV. EDX is conducted at different locations on the surface of the samples to find the average composition across the samples. Table 2 presents the atomic percentage of Nb and Sn in the as-deposited and annealed samples. For the as-deposited samples, the atomic percentage of Sn is 25–33%. Due to Sn evaporation from the surface during annealing, the annealed samples have lower Sn composition. Annealed samples at simulated positions of the SRF cavity equator and bottom beam tube have a Sn composition of ~19%, while the top beam tube has an Sn composition of ~22%. Sn loss during annealing was observed previously in Nb_3Sn fabricated by magnetron multilayer sputtering, where the Sn composition was ~20–24 % after annealing under similar annealing conditions [35].

Table 2. Sn composition and root-mean-square (RMS) roughness of the as-deposited and annealed samples.

Position of sample	Sn composition of as-deposited samples (at. %)	Sn composition of annealed samples (at. %)	RMS roughness as-deposited (nm)	RMS roughness annealed (nm)
Top beam tube	33	22	68	50
Equator	32	19	26	28
Bottom beam tube	25	19	43	50

4.3.3 Surface topography

The surface topography of the samples was examined using a Digital Instrument Dimension 3100 Atomic Force Microscopy (AFM). Figures 6 and 7 show the AFM images of the surfaces of as-deposited and annealed samples. The root-mean-square (RMS) roughness of the as-deposited films for the samples located at the positions of the top beam tube and the bottom beam tube are 68 nm and 43 nm, respectively, whereas the sample at the equator position has an RMS roughness of 26 nm. Due to the proximity of the beam tubes to the sputtering target compared to the equator of the SRF cavity (0.32'' and 1.58'' distance from the surface of the target, respectively), the magnetron plasma might interact with the sputtered film [44]. This results in the higher RMS roughness of the films on the beam tube positions compared to the equator position film. The annealed samples also show the same trend in both films deposited at the beam tube location with a RMS roughness of 50 nm and the film at the equator position having an RMS roughness of 28 nm.

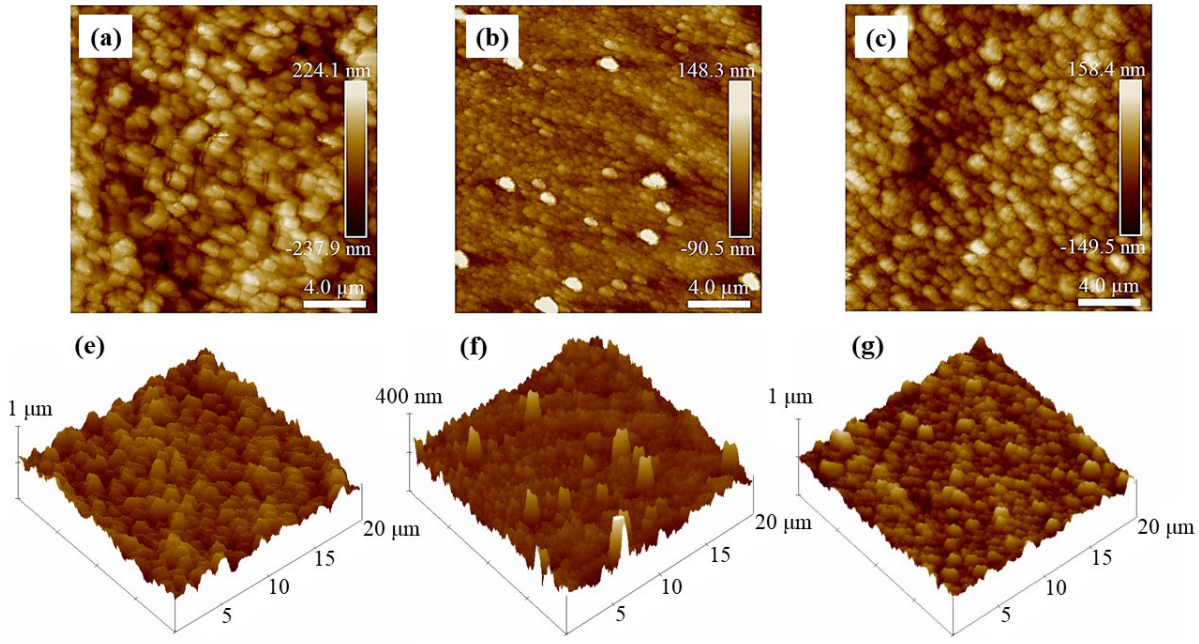

Fig. 6. AFM images of the as-deposited films prepared at equivalent positions of (a) top beam tube, (b) equator, and (c) bottom beam tube of the 2.6 GHz Nb SRF cavity; (d), (e) and (f) are 3D AFM images of (a)–(c), respectively.

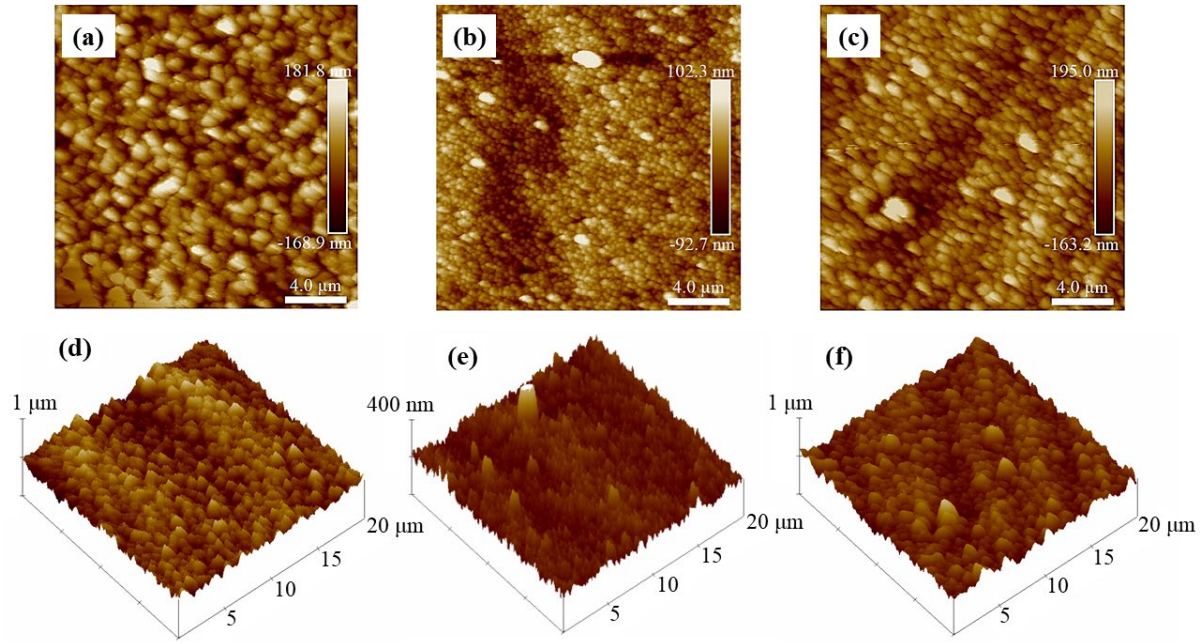

Fig. 7. AFM images of the annealed films prepared at equivalent positions of (a) top beam tube, (b) equator, and (c) bottom beam tube of the 2.6 GHz Nb SRF cavity; (d), (e) and (f) are 3D plots of the AFM images of (a)–(c), respectively.

Surface topography variation is measured from AFM sectional line scans obtained over a 20 µm × 20 µm area. Figure 8 shows that the film at the equator position has a maximum peak-to-valley height difference of ~164 nm. The surface of the samples at the beam tube position shows a maximum height difference of ~240 nm. The smaller peak-to-valley height differences of the film at the equator position shows a smoother surface with an RMS surface roughness of ~28 nm compared to beam tube films having RMS roughness of ~50 nm.

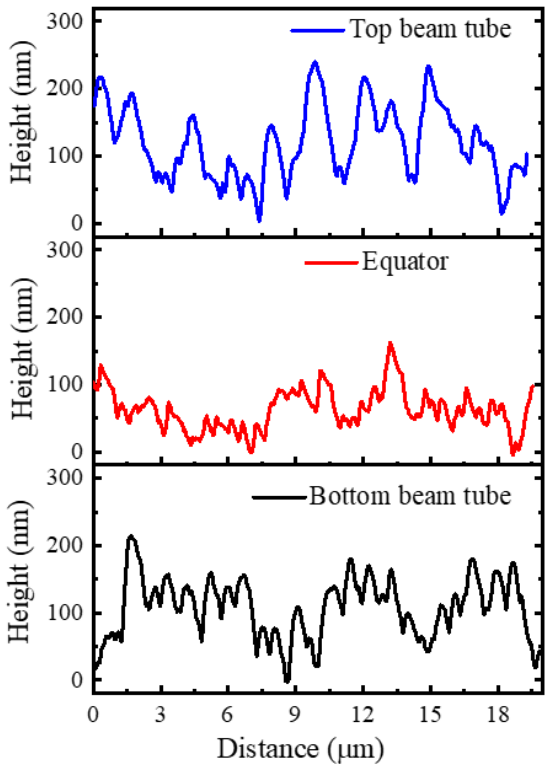

Fig. 8. AFM line scans of the Nb_3Sn films deposited on the Nb substrates that were placed at the positions of the top beam tube, equator, and bottom beam tube of a 2.6 GHz Nb SRF cavity.

4.3.3 Superconducting properties:

Nb_3Sn films were deposited on sapphire substrates mounted on the equivalent positions of the 2.6 GHz Nb cavity's beam tube centers and the equator. These substrates were cut into 1–2 cm^2 pieces from 2" diameter 430-μm thick double-side polished sapphire with C-M orientation obtained from University Wafers Inc. The same multilayer sputter coating procedure and post-deposition annealing used to deposit Nb_3Sn on the flat Nb substrates were followed. The superconducting properties of the Nb_3Sn films on sapphire were investigated by the four-point probe method down to 4 K using the RRR measurement system [45]. This system maintains an isothermal environment inside the liquid helium dewar and measures the sample temperature with a resolution of less than 50 mK through the T_c range of Nb_3Sn

using calibrated Cernox thermometers. The resistivity of the sample is measured by applying a delta pulse using a Keithley model 6221 current source and Keithley model 2181A nano-voltmeter.

Figure 9 shows the normalized resistance versus temperature of the Nb_3Sn films deposited on sapphire. The T_c is the average of two temperatures, T_{90} and T_{10}, which are the temperatures of the sample when the resistance is 90% and 10% of its value at the start of the superconducting transition, respectively. The transition width ΔT_c is the difference between T_{90} and T_{10}. The RRR is calculated from the ratio of film resistivity at 300 K to that at 20 K for the samples at the beam tubes positions and from the measured ratio of the resistance at 275 K to that at 20 K for the sample at the equator position. The values T_c, ΔT_c, and RRR obtained from Figure 9 are listed in Table 3. The superconducting transition of Nb_3Sn was observed for all three films placed at the beam tubes and equator positions of the cavity. The T_c range was 17.61–17.76 K with the highest T_c = 17.76 K and lowest ΔT_c =0.06 K obtained for the film at the equator position.

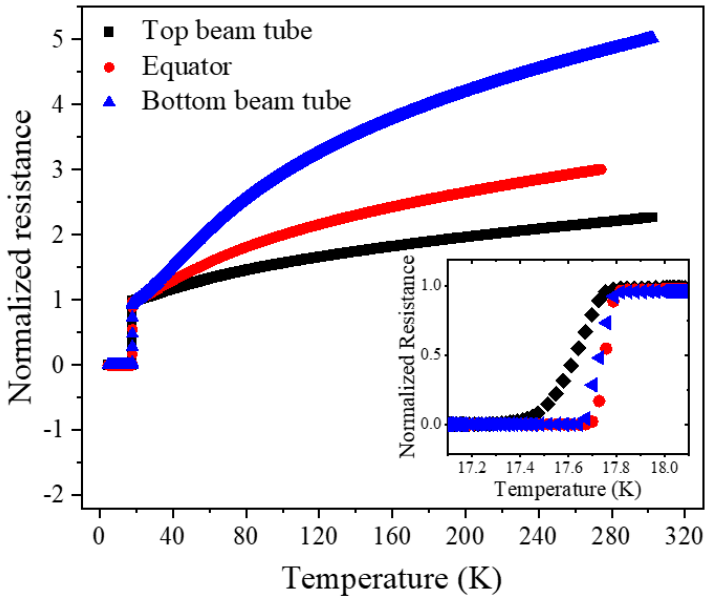

Fig. 9. Resistance versus temperature of the Nb_3Sn films deposited on sapphire at three equivalent positions of a 2.6 GHz Nb cavity. The inset shows the transition region of film resistivity into the superconducting state.

Table 3. Superconducting properties of the Nb_3Sn films deposited at three positions replicating 2.6 GHz Nb SRF cavity.

Positions	T_c (K)	ΔT_c (K)	RRR
Top beam tube	17.61	0.24	2.26
Equator	17.76	0.06	3.00
Bottom beam tube	17.73	0.10	5.01

5. Cavity coating

5.1 Multilayer coating of 2.6 GHz SRF Nb cavity

A scaled TESLA-shape single-cell 2.6 GHz Nb cavities, made from high-purity Nb with RRR ~300, were used in this study [8]. After fabrication and prior to the film deposition, cavities were electropolished for 120 μm in electropolishing solution (HF(70wt%) and H_2SO_4(96wt%) in 1:10 volumetric ratio), annealed at 800 °C for two hours in a high vacuum furnace, and electropolished for 25 μm in EP solution again. Polished cavities were rinsed and assembled for cryogenic testing in ISO4 cleanroom. In cryogenic RF testing cavities exhibited the standard performance expected with the electropolishing preparation, where the maximum field was limited to $E_{acc} \approx 30$ MV/m by the high field Q-slope. The quality factor at low fields was above $7 \cdot 10^9$ at 2.0 K and $8 \cdot 10^{10}$ at 1.4 K. Following the cryogenic RF testing, cavities were disassembled, cleaned, and prepared for film deposition in ISO4 cleanroom.

Fig. 10. 2.6 GHz Nb SRF cavity placed in the cylindrical magnetron-sputtering coating chamber for Nb-Sn multilayer deposition. The top magnetron with its target placed can be seen. The corrugated flexible line to the right is used to supply Ar gas during deposition to the discharge space.

Figure 10 shows the 2.6 GHz Nb SRF cavity inside the chamber for Nb-Sn multilayer deposition. The same deposition conditions and automation program used for Nb_3Sn fabrication on the flat Nb substrates were used for Nb_3Sn coating of the inside surface of the SRF cavity. The coating inside the cavity looked uniform, with no visible film peeling. The coated cavity was then annealed in a separate high vacuum furnace. The furnace features 12” x 12” x 18” hot zone enclosed with molybdenum heat shields. Custom molybdenum covers were assembled onto the cavity flanges prior to annealing and the furnace with the cavity setup was evacuated to $6 \cdot 10^{-7}$ Torr. The hot zone with the cavity was first degassed at about 300 °C for 24 hours. The furnace pressure was about $2 \cdot 10^{-7}$ Torr before the main annealing cycle. The main annealing cycle was done at 950 °C for 3 hours. Figure 11 shows the temperature profile of the

annealing cycle used for the coated cavity. Figure 12 shows the inside picture of the coated cavity surface before and after annealing. A slight variation in appearance inside the cavity after the annealing.

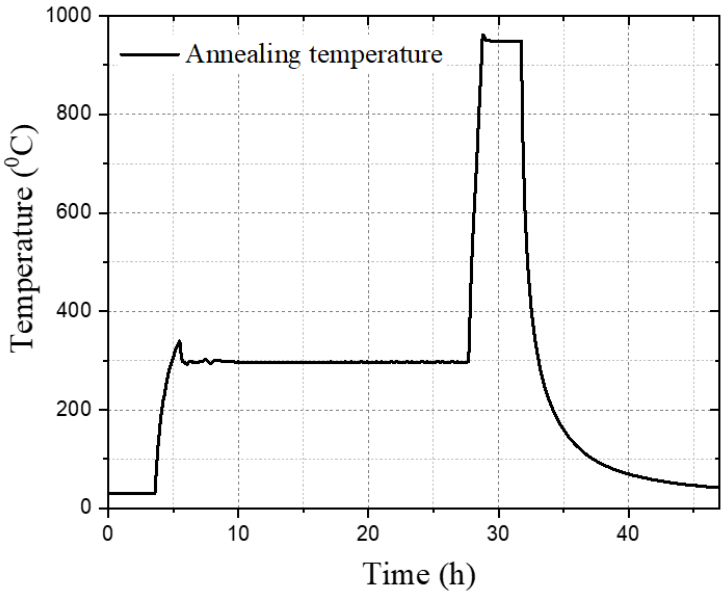

Fig. 11. Temperature profile of the annealing process for the coated cavity. The annealing cycle consists of a degassing phase for 24 hours followed by the main annealing cycle at 950 °C for 3 hours, when Nb-Sn multilayers are converted into Nb_3Sn film.

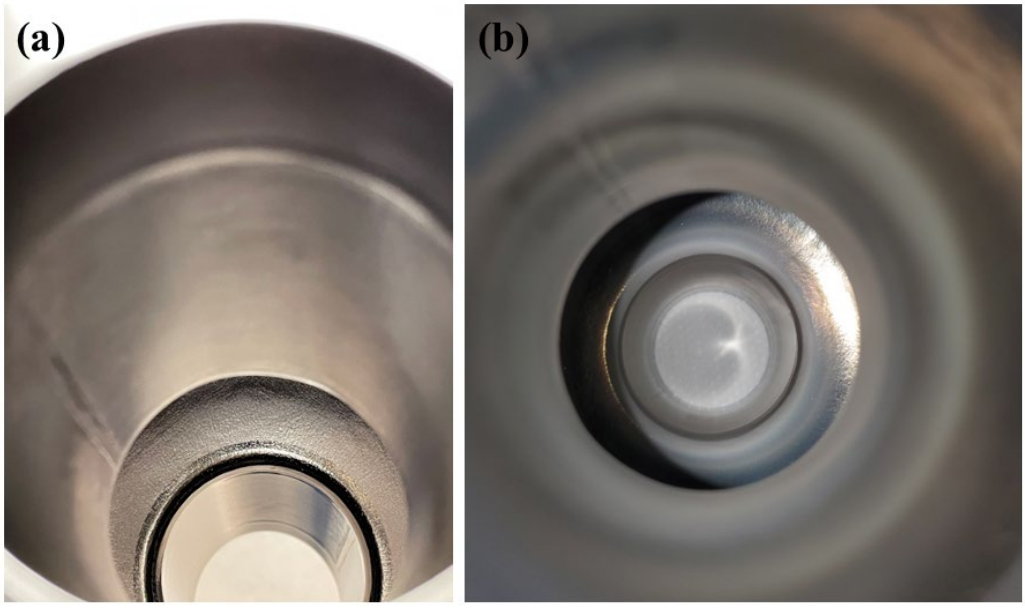

Fig. 12. Pictures of the coated cavity surface (a) as-deposited (b) after annealing at 950 ^{0}C for 3 hours. Note uniform appearance and matte color of Nb_3Sn coating.

5.2. Coated cavity performance

After furnace annealing, the cavity was prepared for cryogenic RF testing in the cleanroom. The cavity did not receive any chemical surface treatment after annealing other than high pressure water rinsing using ultra-high purity water. During cryogenic RF test, the coated cavity demonstrates a quality factor (Q_0) of 3.2 x 10^8 at E_{acc} = 5 MV/m at T_{bath} = 4.4 K and Q_0 of 1.1 x 10^9 at E_{acc} = 5 MV/m at T_{bath} = 2 K, as shown in the Figure 13.

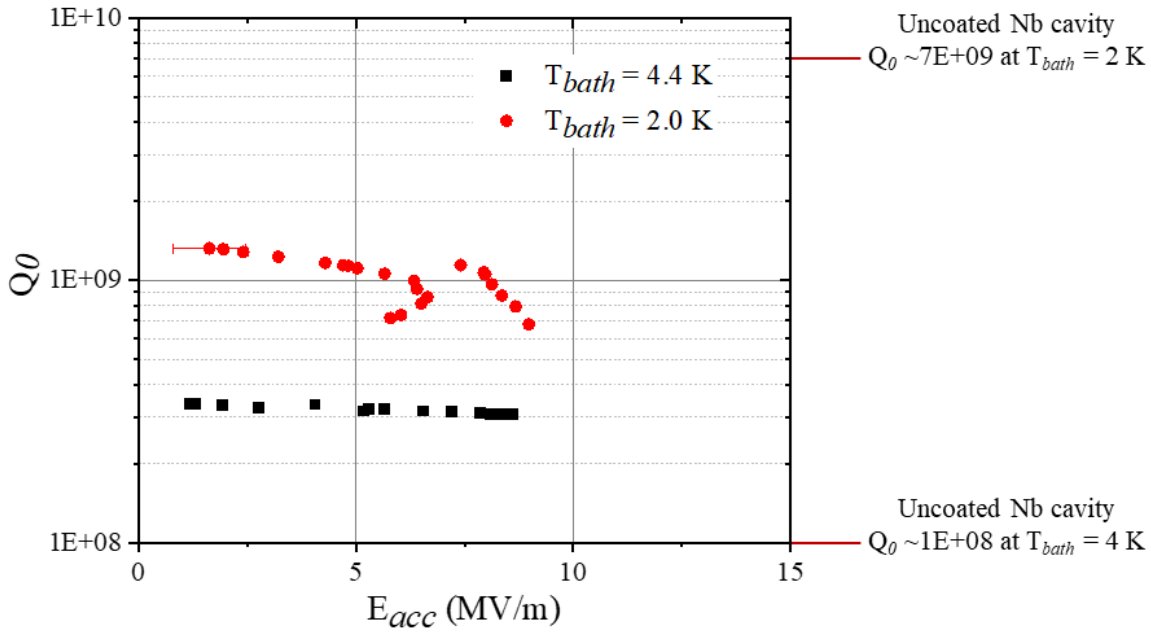

Fig. 13. Q_0 versus E_{acc} at 4.4 K and 2.0 K for the Nb_3Sn-coated 2.6 GHz Nb cavity. For comparison, typical Q_0 values of the uncoated 2.6 GHz niobium cavities at 4 and 2 K are shown.

After high field measurements were completed, a network analyzer was connected to cavity ports to measure cavity Q_0 as a function of temperature. As the temperature of the cavity increased during warm-up, Q_0 of the cavity was continuously measured from the width of the resonant peak in s21 transmission using FWHM technique. The measurement results are shown in Figure 14. As expected for Nb_3Sn, the superconducting transition is seen at about 17.9 K. Another superconducting transition is observed at

about 9.2 K. This transition is likely caused by Nb end flanges used for cryogenic testing of this cavity. Another transition can be noticed at about 8 K. We speculate that there may be Sn-deficient regions close to the ends of the cavity, which cause the transition at 8 K.

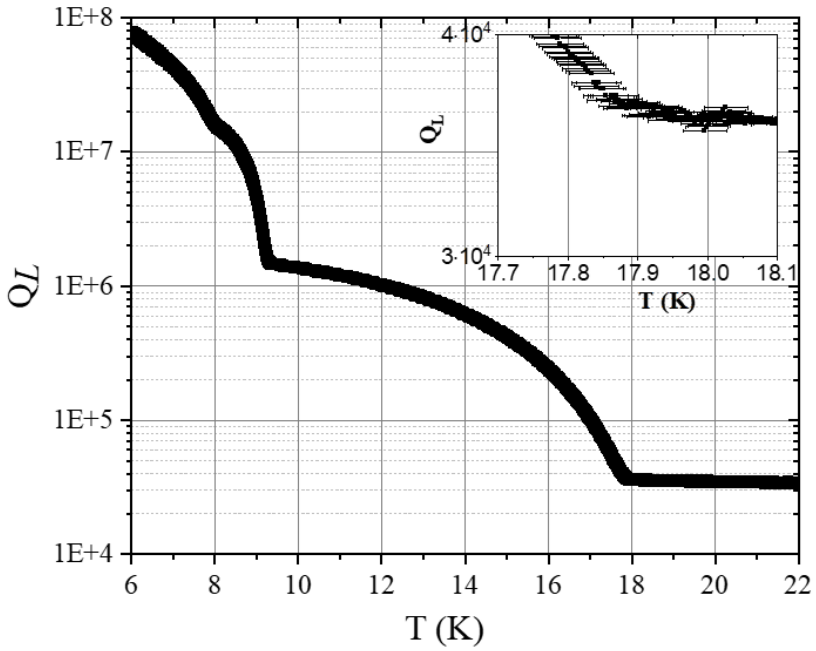

Fig. 14. Q_L versus T data showing the superconducting transition temperature of 17.9 K due Nb_3Sn coating. Two other transitions are seen in the plot at lower temperatures due to uncoated regions.

6. Conclusion

We have designed and commissioned a cylindrical magnetron sputtering coating system capable of coating Nb_3Sn on the inner surface of 2.6 GHz SRF cavities using two identical DC cylindrical magnetrons. A sample holder allows coating on flat Nb or sapphire substrates at positions similar to the equator and beam tubes of 2.6 GHz SRF cavity was used to find optimal conditions to grow Nb_3Sn layers. Nb_3Sn films on the flat samples achieved T_c in the range of 17.61–17.76 K. A similar film was deposited on a 2.6 GHz single-cell Nb cavity for the first time. The coated cavity demonstrated Q_0 of 3.2 x 10^8 at T_{bath} = 4.4 K and Q_0 of 1.1 x 10^9 T_{bath} = 2 K, both at E_{acc} = 5 MV/m with a superconducting transition temperature of 17.9 K. Ongoing work with the DC cylindrical magnetron sputtering system includes

improving the coverage and quality of the Nb_3Sn film on 2.6 GHz Nb SRF cavity using sequential and co-sputtering Nb and Sn.

Acknowledgment

This manuscript is based upon work supported by the U.S. Department of Energy, Office of Science, Office of Accelerator R&D and Production, under contract No. DE-SC0022284 and the U.S. Department of Energy, Office of Science, Office of Nuclear Physics under contract DE-AC05-06OR23177 with Jefferson Science Associates, including supplemental funding via the DOE Early Career Award to G. Eremeev. The manuscript has been authored by Fermi Research Alliance, LLC, under Contract No. DE-AC02-07CH11359 with the U.S. Department of Energy, Office of Science, Office of High Energy Physics. The authors acknowledge David Beverstock of the College of William and Mary for his help with T_c measurement.

References

[1] M. Altarelli, R. Brinkmann, M. Chergui et al. (Eds), XFEL: The European X-Ray Free-Electron Laser, Technical Design Report, DESY 2006-097, DESY, Hamburg, 2007. http://dx.doi.org/10.3204/DESY_06-097.

[2] C.E. Reece, Continuous wave superconducting radio frequency electron linac for nuclear physics research, Phys. Rev. Accel. Beams. 19 (2016) 1–31. https://doi.org/10.1103/PhysRevAccelBeams.19.124801.

[3] J. Stohr, Linac coherent light source II (LCLS-II) conceptual design report, Technical Report, SLAC National Accelerator LaboratoryMenlo Park, CA, 2011. https://doi.org/10.2172/1029479.

[4] M. Ball et al., The PIP-II Conceptual Design Report. United States: N. p., 2017. https://doi.org/10.2172/1346823.

[5] F. Willeke and J. Beebe-Wang, Electron Ion Collider Conceptual Design Report 2021. United States: N. p., 2021. https://doi.org/10.2172/1765663.

[6] Abada, A., Abbrescia, M., AbdusSalam, S.S. et al. FCC-ee: The Lepton Collider. Eur. Phys. J. Spec. Top. 228, 261–623 (2019). https://doi.org/10.1140/epjst/e2019-900045-4.

[7] D. Broemmelsiek, B. Chase, D. Edstrom, E. Harms, J. Leibfritz, S. Nagaitsev, Y. Pischalnikov, A. Romanov, J. Ruan, W. Schappert, V. Shiltsev, R. Thurman-Keup, A. Valishev, Record high-

gradient SRF beam acceleration at Fermilab, New J. Phys. 20 (2018) 113018. https://doi.org/10.1088/1367-2630/AAEC57.

[8] B. Aune, R. Bandelmann, D. Bloess, B. Bonin, A. Bosotti, M. Champion, C. Crawford, G. Deppe, B. Dwersteg, D.A. Edwards, H.T. Edwards, M. Ferrario, M. Fouaidy, P.D. Gall, A. Gamp, A. Gössel, J. Graber, D. Hubert, M. Hüning, M. Juillard, T. Junquera, H. Kaiser, G. Kreps, M. Kuchnir, R. Lange, M. Leenen, M. Liepe, L. Lilje, A. Matheisen, W.D. Möller, A. Mosnier, H. Padamsee, C. Pagani, M. Pekeler, H.B. Peters, O. Peters, D. Proch, K. Rehlich, D. Reschke, H. Safa, T. Schilcher, P. Schmüser, J. Sekutowicz, S. Simrock, W. Singer, M. Tigner, D. Trines, K. Twarowski, G. Weichert, J. Weisend, J. Wojtkiewicz, S. Wolff, K. Zapfe, Superconducting TESLA cavities, Phys. Rev. Spec. Top. - Accel. Beams. 3 (2000) 092001. https://doi.org/10.1103/PhysRevSTAB.3.092001.

[9] H. Padamsee, 50 years of success for SRF accelerators - A review, Supercond. Sci. Technol. 30 (2017) 053003. https://doi.org/10.1088/1361-6668/aa6376.

[10] A. Gurevich, Enhancement of rf breakdown field of superconductors by multilayer coating, Appl. Phys. Lett. 88 (2006) 012511. https://doi.org/10.1063/1.2162264.

[11] J. Matricon, D. Saint-James, Superheating fields in superconductors, Phys. Lett. A. 24 (1967) 241–242. https://doi.org/10.1016/0375-9601(67)90412-4.

[12] A.M. Valente-Feliciano, Superconducting RF materials other than bulk niobium: A review, Supercond. Sci. Technol. 29 (2016) 113002. https://doi.org/10.1088/0953-2048/29/11/113002.

[13] S. Posen, D.L. Hall, Nb_3Sn superconducting radiofrequency cavities: fabrication, results, properties, and prospects, Supercond. Sci. Technol. 30 (2017) 033004. https://doi.org/10.1088/1361-6668/30/3/033004.

[14] U. Pudasaini, G. V. Eremeev, C.E. Reece, J. Tuggle, M.J. Kelley, Initial growth of tin on niobium for vapor diffusion coating of Nb_3Sn, Supercond. Sci. Technol. 32 (2019) 045008. https://doi.org/10.1088/1361-6668/aafa88.

[15] G. Eremeev, W. Clemens, K. Macha, C.E. Reece, A.M. Valente-Feliciano, S. Williams, U. Pudasaini, M. Kelley, Nb_3Sn multicell cavity coating system at Jefferson Lab, Rev. Sci. Instrum. 91 (2020) 073911. https://doi.org/10.1063/1.5144490.

[16] S. Posen, S.K. Chandrasekaran, J. Lee, O. Melnychuk, D. Sergatskov, B. Tennis, Y. Trenikhina, Development of Nb_3Sn Coatings for Superconducting RF Cavities at Fermilab, Proc. 9th Int. Part. Accel. Conf. (2018) 2718–2720. https://doi.org/10.18429/JACOW-IPAC2018-WEPML016.

[17] Y. Trenikhina, S. Posen, A. Romanenko, M. Sardela, J.M. Zuo, D.L. Hall, M. Liepe, Performance-defining properties of Nb_3Sn coating in SRF cavities, Supercond. Sci. Technol. 31 (2017) 015004. https://doi.org/10.1088/1361-6668/AA9694.

[18] C.A. Neugebauer, Thin Films of Niobium Tin by Codeposition, J. Appl. Phys. 35 (2004) 3599. https://doi.org/10.1063/1.1713278.

[19] S.M. Deambrosis, G. Keppel, V. Ramazzo, C. Roncolato, R.G. Sharma, V. Palmieri, A15 superconductors: An alternative to niobium for RF cavities, Phys. C Supercond. 441 (2006) 108–113. https://doi.org/10.1016/J.PHYSC.2006.03.047.

[20] E. Barzi, M. Bestetti, F. Reginato, D. Turrioni, S. Franz, Synthesis of superconducting Nb_3Sn coatings on Nb substrates, Supercond. Sci. Technol. 29 (2015) 015009. https://doi.org/10.1088/0953-2048/29/1/015009.

[21] S. Franz, E. Barzi, D. Turrioni, L. Glionna, M. Bestetti, Electrochemical synthesis of Nb_3Sn coatings on Cu substrates, Mater. Lett. 161 (2015) 613–615. https://doi.org/10.1016/J.MATLET.2015.09.046.

[22] K. Zhang, P. Zhang, J. Guo, J. Jia, Y. Shi, J. Liu, H. Gao, J. Li, X. Liu, Y. Feng, Study and Manufacture of Nb_3Sn Strands by Bronze Route, IEEE Trans. Appl. Supercond. 26 (2016) 6000904. https://doi.org/10.1109/TASC.2016.2530870.

[23] L. Zhu, X. Lu, Z. Yang, W. Tan, Y. Yang, L. Xiao, D. Xie, Study on preparation of Nb_3Sn films by bronze route, Phys. C Supercond. Its Appl. 601 (2022) 1354113. https://doi.org/10.1016/J.PHYSC.2022.1354113.

[24] M.N. Sayeed, U. Pudasaini, G. V. Eremeev, H.E. Elsayed-Ali, Fabrication of superconducting Nb_3Sn film by Co-sputtering, Vacuum 212 (2023) 112019. https://doi.org/10.1016/j.vacuum.2023.112019.

[25] E.A. Ilyina, G. Rosaz, J.B. Descarrega, W. Vollenberg, A.J.G. Lunt, F. Leaux, S. Calatroni, W. Venturini-Delsolaro, M. Taborelli, Development of sputtered Nb_3Sn films on copper substrates for superconducting radiofrequency applications, Supercond. Sci. Technol. 32 (2019) 035002. https://doi.org/10.1088/1361-6668/aaf61f.

[26] M.N. Sayeed, U. Pudasaini, C.E. Reece, G.V. Eremeev, H.E. Elsayed-Ali, Properties of Nb_3Sn films fabricated by magnetron sputtering from a single target, Applied Surface Science 541 (2021) 148528. https://doi.org/10.1016/j.apsusc.2020.148528.

[27] G. Rosaz, S. Calatroni, F. Leaux, F. Motschmann, Z. Mydlarz, M. Taborelli, W. Vollenberg, G. Switzerland, Development of Nb_3Sn coatings by magnetron sputtering for SRF cavities, Proceedings of 17th International Conference on RF Superconductivity (2015) TUPB051. https://doi.org/10.18429/JACoW-SRF2015-TUPB051.

[28] M.S. Shakel, W. Cao, H.E. Elsayed-Ali, M.N. Sayeed, U. Pudasaini, A.M. Valente-Feliciano Thomas Jefferson, Nb_3Sn coating of a 2.6 GHz SRF cavity by sputter deposition technique, Proceedings of 5th North American Particle Accel. Conf. (2022) WEPA30. https://doi.org/10.18429/JACoW-NAPAC2022-WEPA30.

[29] N. Schäfer, N. Karabas, J.P. Palakkal, S. Petzold, M. Major, N. Pietralla, L. Alff, Kinetically induced low-temperature synthesis of Nb_3Sn thin films, J. Appl. Phys. 128 (2020) 133902. https://doi.org/10.1063/5.0015376.

[30] M.N. Sayeed, U. Pudasaini, C.E. Reece, G. Eremeev, H.E. Elsayed-Ali, Structural and superconducting properties of Nb_3Sn films grown by multilayer sequential magnetron sputtering, J. Alloys Compd. 800 (2019) 272–278. https://doi.org/10.1016/j.jallcom.2019.06.017.

[31] R. Valizadeh, A.N. Hannah, S. Aliasghari, O.B. Malyshev, G.B.G. Stenning, D. Turner, K. Dawson, V.R. Dahnak, PVD Depostion of Nb_3Sn Thin Film on Copper Substrate from an Alloy Nb_3Sn Target, Proc. of 10th Int. Particle Accelerator Conf. (2019). https://doi.org/10.18429/JACoW-IPAC2019-WEPRB011.

[32] S. Posen, M. Liepe, D.L. Hall, Proof-of-principle demonstration of Nb_3Sn superconducting radiofrequency cavities for high Q_0 applications, Appl. Phys. Lett. 106 (2015) 082601. https://doi.org/10.1063/1.4913247.

[33] U. Pudasaini, G. Eremeev, C.E. Reece, J. Tuggle, M.J. Kelley, Surface studies of Nb_3Sn coated samples prepared under different coating conditions, Proceedings of 18th International Conference on RF Superconductivity (2017) THPB069. https://doi.org/10.18429/JACoW-SRF2017-THPB069.

[34] J. Lee, S. Posen, Z. Mao, Y. Trenikhina, K. He, D.L. Hall, M. Liepe, D.N. Seidman, Atomic-scale analyses of Nb_3Sn on Nb prepared by vapor diffusion for superconducting radiofrequency cavity applications: a correlative study, Supercond. Sci. Technol. 32 (2018) 024001. https://doi.org/10.1088/1361-6668/AAF268.

[35] C. Becker *et al.*, "Analysis of Nb3Sn surface layers for superconducting radio frequency cavity applications," *Appl. Phys. Lett.*, vol. 106, no. 8, pp. 1–5, 2015. https://doi.org/10.1063/1.4913617

[36] M.N. Sayeed, U. Pudasaini, C.E. Reece, G. V. Eremeev, H.E. Elsayed-Ali, Effect of layer thickness on structural, morphological and superconducting properties of Nb3Sn films fabricated by multilayer sequential sputtering, IOP Conf. Ser. Mater. Sci. Eng. 756 (2020) 012014. https://doi.org/10.1088/1757-899X/756/1/012014.

[37] A. le Febvrier, L. Landälv, T. Liersch, D. Sandmark, P. Sandström, P. Eklund, An upgraded ultra-high vacuum magnetron-sputtering system for high-versatility and software-controlled deposition, Vacuum 187 (2021) 110137. https://doi.org/10.1016/j.vacuum.2021.110137.

[38] A. Anders, R. Mendelsberg, S. Lim, M. Mentink, J.L. Slack, J.G. Wallig, Deposition of Niobium and other superconducting materials with high power impulse magnetron sputtering: Concept and first results, Proceedings of 15th International Conference on RF Superconductivity (2011) TUIOA06. https://accelconf.web.cern.ch/SRF2011/papers/tuioa06.pdf.

[39] G. Terenziani, S. Calatroni, T. Junginger, I.A. Santillana, S. Sheffield, Nb coating developments with HIPIMS for SRF Applications, Proceedings of the 16th International Conference on RF Superconductivity (2013) TUP078. https://doi.org/10.13140/2.1.4279.7765.

[40] C. Benvenuti, N. Circelli, and M. Hauer, Niobium films for superconducting accelerating cavities. United States: N. p., 1984. https://doi.org/10.1063/1.95289.

[41] G. Rosaz, A. Bartkowska, C.P.A. Carlos, T. Richard, M. Taborelli, Niobium thin film thickness profile tailoring on complex shape substrates using unbalanced biased High Power Impulse Magnetron Sputtering, Surf. Coatings Technol. 436 (2022) 128306. https://doi.org/10.1016/j.surfcoat.2022.128306.

[42] M.N. Sayeed, H.E. Elsayed-Ali, G. V Eremeev, A.M. Valente-Feliciano, T. Jefferson, C. Côté, M. Farzad, M. Patterson, A. Chang, A. Sarkissian, Cylidrical magnetron development for Nb_3Sn deposition via magnetron sputtering, Proc. of 20th Int. Conf. on RF Superconductivity (2021), 868–870, THPTEV015. https://doi.org/10.18429/JACoW-SRF2021-THPTEV015.

[43] N. Sayeed, H. E. Elsayed-Ali, U. Pudasaini, G. V Eremeev, C.E. Reece, M. Burton, A.M. Valente-Feliciano, Deposition of Nb_3Sn films by multilayer sequential sputtering for SRF cavity application, Proceedings of 19th Int. Conf. on RF Superconductivity (2019) 637-641, TUP079. https://doi.org/10.18429/JACoW-SRF2019-TUP079.

[44] P.A. Cormier, A.L. Thomann, Vincent Dolique, A. Balhamri, Remi Dussart, Nadjib Semmar, Thomas Lecas, Pascal Brault, R. Snyders, and Stephanos Konstantinidis, IR emission from the target during plasma magnetron sputter deposition, Thin Solid Films 545 (2013) 44-49. https://doi.org/10.1016/j.tsf.2013.07.025.

[45] J.K. Spradlin, C.E. Reece, A.-M. Valente-Feliciano, A multi-sample residual resistivity ratio system for high quality superconductor measurements, Proceedings of 17th International Conference on RF Superconductivity (2015) TUPB063. https://doi.org/10.18429/JACoW-SRF2015-TUPB063.